ADVANCED INTELLIGENT SYSTEMS Open Access
www.advintellsyst.com

Bidirectional Propulsion of Arc-Shaped Microswimmers Driven by Precessing Magnetic Fields

Sumit Mohanty, Qianru Jin, Guilherme Phillips Furtado, Arijit Ghosh, Gayatri Pahapale, Islam S. M. Khalil, David H. Gracias, and Sarthak Misra*

We would like to dedicate this work to Guilherme Phillips Furtado who tragically passed away during the preparation of the manuscript

The development of magnetically powered microswimmers that mimic the swimming mechanisms of microorganisms is important for lab-on-a-chip devices, robotics, and next-generation minimally invasive surgical interventions. Governed by their design, most previously described untethered swimmers can be maneuvered only by varying the direction of applied rotational magnetic fields. This constraint makes even state-of-the-art swimmers incapable of reversing their direction of motion without a prior change in the direction of field rotation, which limits their autonomy and ability to adapt to their environments. Also, due to constant magnetization profiles, swarms of magnetic swimmers respond in the same manner, which limits multiagent control only to parallel formations. Herein, a new class of microswimmers are presented which are capable of reversing their direction of swimming without requiring a reversal in direction of field rotation. These swimmers exploit heterogeneity in their design and composition to exhibit reversible bidirectional motion determined by the field precession angle. Thus, the precession angle is used as an independent control input for bidirectional swimming. Design variability is explored in the systematic study of two swimmer designs with different constructions. Two different precession angles are observed for motion reversal, which is exploited to demonstrate independent control of the two swimmer designs.

1. Introduction

There exist motile microorganisms such as bacteria and sperm cells that adopt versatile swimming mechanisms to improve their mechanical efficiency, regardless of the rheological characteristics of their environment. They are known to tackle obstacles in drag-dominated viscous media, thereby facilitating complex biological functions.[1] Notably, many species of bacteria undergo polymorphic transformations with their flagellar appendages to propel themselves forward and backward.[2–5] Akin to bacteria, sperm cells have been reported to swim backwards in the female reproductive tract to fertilize an egg.[6–9] Inspired by nature, many ingenious artificial[10–12] and biohybrid microswimmers[13–15] have been engineered to mimic these cellular biological microorganisms and imitate their motion at low Reynolds numbers. The most prolific of these are helical magnetic micro- and nano swimmers that readily align their tails in response to time-varying magnetic fields that cause them to propel forward.[16–18]

Advances in microfabrication have enabled the construction of microswimmers which can reconfigure their morphology to achieve locomotion in confined workspaces.[19,20] However, many of these previously developed microswimmers lack the ability to actively reverse their magnetic anisotropy while in motion. Hence, these swimmers cannot readily reverse their swimming direction like bacteria or sperm cells, without a prior simultaneous reversal in the direction of the applied magnetic field. This inability limits their utility under certain robotic or clinically relevant scenarios. Specifically,

S. Mohanty, G. P. Furtado,[+] Dr. I. S. M. Khalil, Prof. S. Misra
Department of Biomechanical Engineering
University of Twente
Drienerlolaan 5, Enschede 7522, NB, The Netherlands
E-mail: s.mohanty@utwente.nl

The ORCID identification number(s) for the author(s) of this article can be found under https://doi.org/10.1002/aisy.202000064.

[+]Deceased

Dr. Q. Jin, Dr. A. Ghosh, G. Pahapale, Prof. D. H. Gracias
Department of Chemical and Biomolecular Engineering
Johns Hopkins University
Baltimore, MD 21218, USA

Prof. D. H. Gracias
Department of Material Science and Engineering
Johns Hopkins University
Baltimore, MD 21218, USA

Prof. S. Misra
Department of Biomedical Engineering
University Medical Centre Groningen
University of Groningen
Groningen 9713, AV, The Netherlands

© 2020 The Authors. Published by WILEY-VCH Verlag GmbH & Co. KGaA, Weinheim. This is an open access article under the terms of the Creative Commons Attribution License, which permits use, distribution and reproduction in any medium, provided the original work is properly cited.

DOI: 10.1002/aisy.202000064

one-tailed microswimmers have to flip themselves to reverse their direction, which is not possible in constricted channels with a shorter width than their body length.[21] Elsewhere, helical microswimmers that can readily reverse their direction upon changing the direction of magnetic rotation cannot be controlled individually when multiple swimmers are steered in unison.[16,22] This limitation prohibits the swimmers from performing cooperative tasks as they continue to move in parallel formations, and are thus incapable of dynamic self-organization. To address this limitation, many microswimmers have been reengineered to incorporate heterogeneous or anisotropic designs to achieve motion differentiation in response to a common driving external stimulus.[23–25] For instance, departing from the conventional design of a sperm cell, a two-tailed microswimmer was reported with the ability to propel back and forth, based on the resonant frequency of planar oscillating magnetic fields.[23,26] While the two-tailed design imparts the swimmer heterogeneity for bidirectional swimming, the swimmer propels with a significantly low velocity compared with its dimension (up to 0.11 body lengths second^{-1}).[23] In contrast, flagellar kinematics of bacteria have also been explored to find correlations between their geometry and the consequential motile behavior.[27–29] Notably, the flagella of a bacterium has been reported to actively participate in both advancing its cell body forward and pulling it backward in a competing fashion.[29] Consequently, bacteria can actively switch between forward and backward propulsion. Moreover, the tilt of the bacterial cell body to its flagellum has also been reported to enhance their swimming velocity in either direction.[28] Inspired by this cellular morphology, a microswimmer with a tilted flagellar appendage has been reported to switch to backward swimming motion under varying frequencies of rotating magnetic fields.[25] This observation is premised upon the swimmer's precessing head competing against its flagellum, as both of them try to inscribe helical trajectories of different radii and chirality.[25] Alternatively, in case of the planar motion of a photoactuated swimmer, motion reversal has been attributed to the phase difference of oscillation between the head and the flagellum.[30]

Inspired by the bacterial morphology, in this work, we design asymmetric arc-shaped microswimmers with a tilted head–flagellum geometry and demonstrate their capability to swim forward and backward by the application of precessing magnetic fields. We analyze the observed motion reversal to be premised upon the different beating patterns of the head and the flagellum. This physical property of our swimmer manifests into a difference in phase and amplitude of rotation for the two respective constituents. Moreover, the motion reversal occurs independent of the direction of the applied magnetic field rotation and its frequency. Thus, the precession angle of the field serves as an important input for motion control. Furthermore, we demonstrate that two swimmer designs with different head–flagellum tilts but the same material composition result in two different precession angles for motion reversal. Finally, we utilize the precession-induced motion reversal of the swimmers to achieve independent motion control of two different microswimmers. Thereby, our approach provides a new basis to achieve motion differentiation in magnetic microswimmers, synthesized with the same material composition. As a result, our findings contribute to the state-of-the-art fabrication methods premised upon photolithography, by achieving functionally dissimilar swimmers with batch fabrication.

2. Results and Discussions

In this work, we describe an asymmetric microswimmer with a rigid triangular head attached to a long flexible flagellum, with a tilt angle between the two components. In addition to the asymmetry in geometry and rigidity, we also introduce a heterogeneous magnetic composition by having a higher magnetization volume in the swimmer's head than the flagellum. These unique features in our swimmers provide them the scope for dynamic reconfiguration around their principal axis when subjected to the changing precession of rotation. Consequently, the application of precessing fields on our swimmers can decouple the two effects, i.e., 1) precession-driven alignment and 2) rotation along the long axis of the swimmer's body.[24] Therefore, we can effectively exploit the precession angle of the field as an additional degree of motion control. We propose that a change in field precession results in different spatial conformations of the head and flagellum, as shown in **Figure 1**a,b, which alter the swimmer's behavior to induce a motion reversal. Moreover, the tilt angle between the swimmer's head and flagellum also determines the extent to which it synchronizes with the changing field precession angle. To measure this variability, we investigate two different designs, with the tilt angle of 30° (Type I) and 45° (Type II), as shown in Figure 1c,d, respectively. These design specifications are inspired by a study on bacterial flagellar kinematics that reports optimal swimming with a body–flagellum tilt close to a 40°–50° range.[28] We thus chose the design metrics closer to these values for our experimental investigation. Herein, we extensively study the aforementioned swimmer designs and characterize their velocities in either direction by varying both the precession angle of the applied field and its frequency.

2.1. Design of Asymmetric Microswimmer

Inspired by curved and rod-shaped bacteria,[28,29] we propose an asymmetric arc-shaped microswimmer design. Fabricated using photolithography and thin-film deposition,[31,32] the swimmer features asymmetry in geometry, rigidity, and magnetization between the two components: the head and the flagellum. The head is a rigid triangle with an aspect ratio of 1:2 and total thickness of 200 nm. The long flagellum has an aspect ratio of 1:30, total thickness of 140 nm, with lower iron proportion than the head. In addition, we design two variants with different tilt angles to examine the influence of the geometrical configuration of the respective components. These variants, namely Type I and Type II, possess the head–flagellum tilt of 30° and 45°, respectively, as shown in Figure 1c,d. Hereon, we focus on characterizing the motion of the Type II swimmer first and later provide a comparison between these two swimmer variants. After fabrication, the swimmers are released from the substrate by dissolving a Cu sacrificial layer using ammonium persulfate (APS) solution, to suspend the swimmers in water. The stress difference in the SiO/SiO_2 bilayer in the flagellum ensures that the swimmers acquire a bilateral deformation and thus form an arc shape upon their release. The effective tip-to-tip length and arc radius of the

© 2020 The Authors. Published by WILEY-VCH Verlag GmbH & Co. KGaA, Weinheim

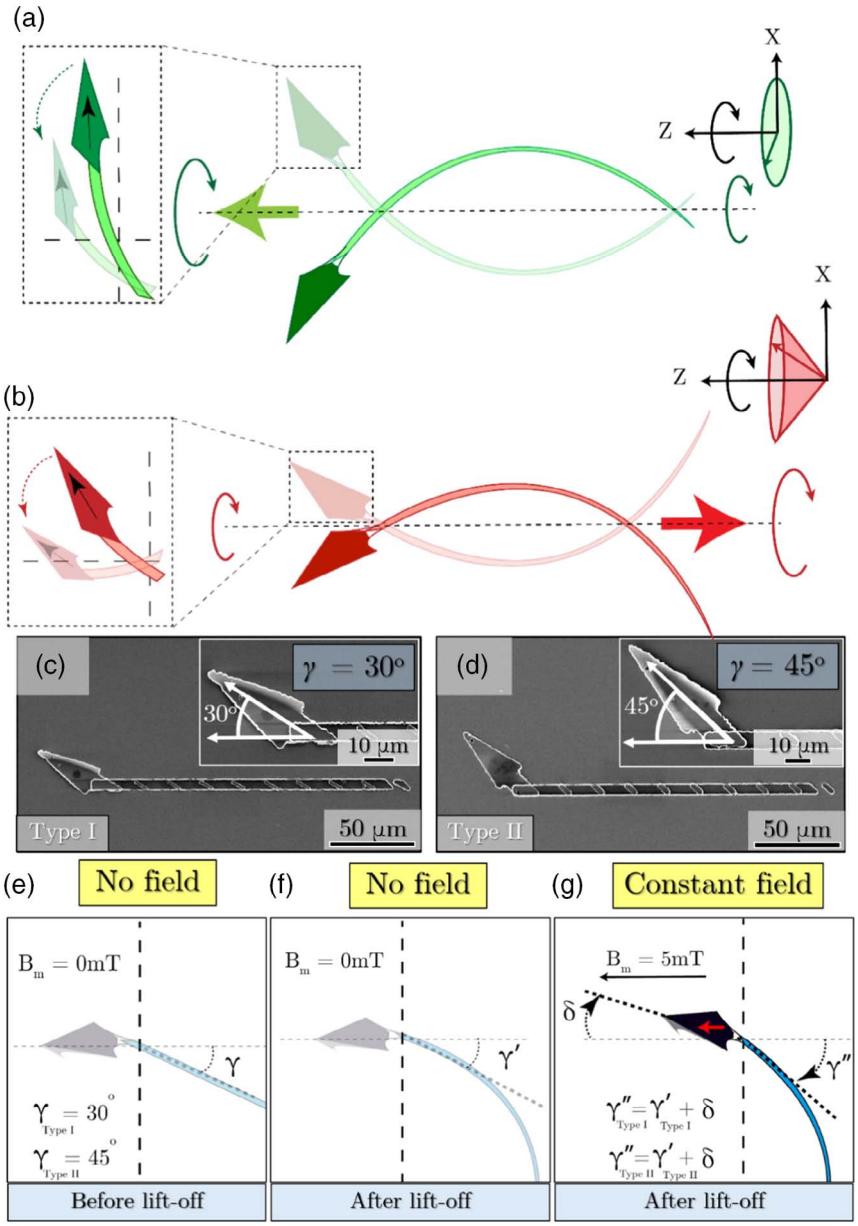

Figure 1. a,b) Schematics of the arc-shaped microswimmer in motion with consecutive swimming strokes superimposed on each other. a) The shape of the swimmer with its triangular-shaped head pitching forward, with a purely cylindrical magnetic field. b) The shape of the swimmer with its flagellum pitching forward, with a magnetic field applied at lower precession angles. c,d) SEM images of the two swimmer geometries, namely, c) Type I and d) Type II, with head–body tilts (γ) of 30° and 45° shown in their respective insets. e–g) The orientation of the swimmer in the e) absence of field before lift-off, f) after lift-off, and g) under a constant magnetic field ($B = 5$ mT). The net dipole moment of the swimmer is marked with a red arrow.

Table 1. Dimensions and easy-axis alignment of the swimmer.

Swimmer	Head–flagellum tilt γ' [°]	Magnetic misalignment δ [°]	Tip-to-tip length [μm][a)]	Arc radius [μm][a)]
Type I	36.0 ± 3.0 ($\gamma = 30$)	9.0 ± 3.2	186.5 ± 7.4	157.3 ± 12.7
Type II	61.3 ± 2.9 ($\gamma = 45$)	17.2 ± 5.7	175.5 ± 4.5	141.6 ± 6.3

[a)]Length of the swimmer (l) and radius (r) are shown in Figure S1, Supporting Information.

swimmer following its release are shown in **Table 1**. The magnetic actuation of the swimmer is achieved using a three-pair Helmholtz coil system that provides uniform rotational magnetic field at its center. A detailed description of the fabrication procedure and experimental setup can be found in the Experimental Section.

Importantly, due to its geometry and higher iron content than the flagellum, the head dominates the magnetic moment of the entire microswimmer. This dominant magnetic head ensures that it preferentially aligns with the precessing magnetic field, and thus the flagellum, due to its tilt, precesses differently with

© 2020 The Authors. Published by WILEY-VCH Verlag GmbH & Co. KGaA, Weinheim

the varying precession angle of the field. We verified this behavior by subjecting the swimmer to a static magnetic field to determine its easy axis and found that the head aligned well with the field. To assess the variance in easy-axis orientation of the swimmer, we define a magnetic misalignment angle to be the angular difference between the orientation of the swimmer's triangular-shaped head and its net magnetic moment (marked red), denoted as δ in Figure 1g. In addition to the magnetic misalignment δ, we introduced two more geometric parameters. Before lift-off, the original tilt angle between the head and flagellum is denoted as γ, which equals 30° for Type I and 45° for Type II (Figure 1e). After lift-off, the angle between the head and the flagellum changes slightly due to the extra curvature introduced by stress in the bilayer, denoted by γ' (Figure 1f). Table 1 shows the post release angle γ' and the magnetic misalignment angle (δ) with respect to a constant field (5 mT). We will later discuss in detail how these parameters affect the motion under the precessing field.

2.2. Reversible Motion and Theoretical Discussion

Our investigation begins with a control experiment to observe vertical motion and the corresponding flagellar deformations of a selected Type II swimmer under the precessing magnetic field ($B = 4$ mT, $f = 3$–4 Hz, and $\theta = 50°$–$90°$). We first apply the precessing field at an angle (θ) of 90° (purely cylindrical). We observe that the swimmer moves with its head inscribing a larger amplitude of rotation than that of the flagellum, as it moves vertically. As we tilt the vertical axis of the applied field, i.e., the pitch angle to 45°, we observe that the swimmer moves in a forward direction. Correspondingly, for this tilted pitch, the swimmer moves vertically upward as its head moves away from the focused imaging plane at a field precession angle of $\theta = 90°$, as shown in Movie S1, Supporting Information. Next, we gradually lower the field precession angle θ to find that the head precesses with a decreasing amplitude. Simultaneously, the flagellum rotates with an increasing amplitude, as shown in **Figure 2**a, and the swimmer transitions to a backward motion upon tilting the vertical pitch (Movie S1, Supporting Information). The lateral displacements of the swimmer pitched at a vertical angle of 45° suggest that its back and forth motion is not due to gravity (Movie S1, Supporting Information). Moreover, as we explore the lateral motion of our swimmer in the range of $\theta = 70°$–$80°$, we observe a transitional phase where no net motion occurs (Movie S1, Supporting Information). In addition to these observations, the beating of the flagellum as θ is varied from 90° to 70° appears to be different. We delineate further into this observation by representing the trajectory inscribed by the head and flagellum, respectively, in polar coordinates. Hereby, we decouple the radial amplitude (ρ) of oscillation and phase of rotation (Φ) for both the head and flagellum in the X–Y plane of rotation. Thus, the rotational phase (Φ) provides the relative phase difference between the head and flagellum, as shown in Figure 2b. At low precession angles, $\theta = 50°$–$60°$, the flagellum leads the head by a fixed phase angle, i.e., $\Phi_h - \Phi_f < 0$. As θ increases from 60° to 90°, we observe that the flagellum encounters a phase crossover and begins to have a phase lag with respect to the head i.e., $\Phi_h - \Phi_f > 0$. Correspondingly, the amplitudes of oscillation ρ for the head ("blue") and flagellum ("red") vary considerably for changing values of θ, as shown in Figure 2b (inset), specifically, the oscillatory pattern of flagellum transitions from circular ("orange") at $\theta = 50°$ to planar in x-axis ("yellow") at $\theta = 70°$ and eventually planar in y-axis ("green") at $\theta = 90°$ (Figure 2b, inset). As a result, the field precession angle forces the swimmer to

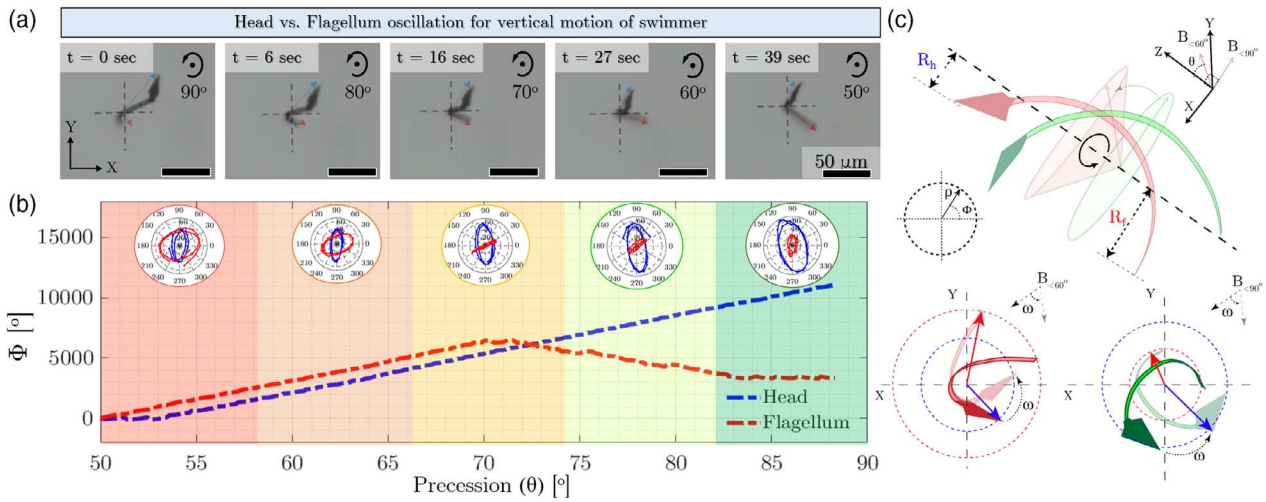

Figure 2. a) Time-lapse images of a Type II microswimmer pitching in the vertical motion under varying precessions of the applied magnetic field ($B = 4$ mT) at a constant frequency ($f = 3$ Hz). b) Polar projection of the trajectory inscribed by the head ("blue") and flagellum ("red") of a Type II microswimmer under precessing magnetic field ($B = 4$ mT) at a constant frequency ($f = 4$ Hz). The plot represents the polar phase coordinate Φ of the two components, and the insets show their respective radial projections ρ for the continuously changing precession angle θ of the magnetic field rotation. c) The schematic shows the swimmer in a precessing field (field magnitude $B_{\angle\theta}$, frequency ω, and precession angle $\theta = 60°$ or 90°). The side profile of the swimmer ("top") shows R_h and R_f as the radial amplitude of oscillations of the head and the flagellum of the swimmer with respect to its principal axis of rotation. The top view of the swimmer described in (a) is represented for two cases of the precessing field with $B_{\angle 90°}$ ("bottom right") and $B_{\angle 60°}$ ("bottom left"). Blue and red arrows show R_h and R_f for the two cases, respectively.

© 2020 The Authors. Published by WILEY-VCH Verlag GmbH & Co. KGaA, Weinheim

exhibit variable beating patterns premised upon two visibly different configurations. At $\theta = 90°$, the head precesses with a longer appendage, akin to an arc leaning forward (Figure 2c, "top," "bottom-right panel," indicated by green color). While at $\theta = 60°$, the flagellum precesses with a longer appendage, akin to an arc leaning backward (Figure 2c, "top," "bottom-left panel," indicated by red color). We attribute this behavior to a change in the relative direction of oscillation of the flagellum with respect to the head, as the field precession changes from $\theta = 70°$–$80°$ (Movie S1, Supporting Information). Here, even though the flagellum makes a nearly planar rotational motion, its direction of rotation is opposite to that of the head, as θ reaches close to 80°, which is indicated by stop points in Movie S1, Supporting Information. A similar observation has been made with the bidirectional behavior of bacteria where its head and flagellum rotate in different patterns.[25,29]

Due to the heterogeneity in our design, the dominant magnetic head of our swimmer can orient itself to the changing field precession angle. Thereafter, the tilted attachment of the head enforces the flexible flagellum to align and eventually follow the rotational field. Second, as the flagellum is also magnetic, it encounters the competing influence of the magnetic torque and retarding torque due to drag forces along its body. When the precession angle of the field is changed, the balance between the magnetic torque and drag torque is disturbed, which gives rise to different deformations in the flexible flagellum. As a result, the flagellum changes its beating pattern between planar and helical whereas the head always maintains a helical trajectory. Hence, the arc-shaped deformation of the flexible flagellum ensures that the swimmer does not drift from its principal axis of rotation, unlike rigid swimmers under precessing fields.[24] In the next section, we further analyzed the swimmer trajectories to quantitatively study the patterns of motion and correlate the resulting phase changes with the swimmer velocity.

2.3. Phase Analysis of Swimmer Motion

Traditionally, flagellar propulsion has been modelled as a bending wave propagating from the swimmer's head toward the flagellum.[1,23,31,33] The direction of flagellar propulsion depends on that of the induced wave propagation along the swimmer's body. Wave propagation in turn is characterized by two components: 1) amplitude of deformation along the swimmer's body and 2) phase difference between different parts of the swimmer's body.[30] Given a constant angle of field precession, the rotational motion of our swimmer causes its head and flagellum to oscillate with different amplitudes and a fixed phase difference between them. When the swimmer is subjected to a change in the field precession angle, the head and flagellum undergo changes in these two characteristics. First, the relative difference in their oscillatory amplitudes changes as the swimmer reverses its motion, akin to the reported observation by Huang et al.[25] Second, we find that under changing field precession, the flagellum shows different beating patterns, which manifest into different phase differences between the head and the flagellum.

To show the relative motion of the head and the flagellum, we resolve the trajectories previously described in polar form (ρ, Φ)

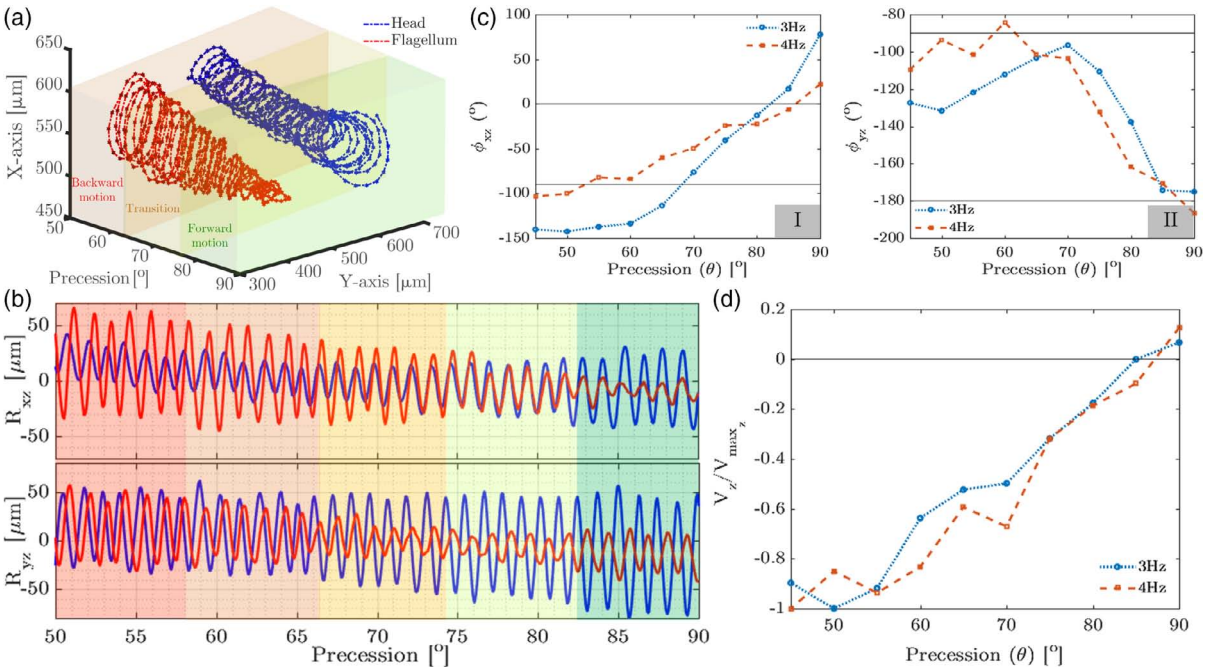

Figure 3. a) A plot of the trajectory inscribed by the head ("blue") and flagellum ("red") of the swimmer moving in the *Z*-direction, as shown in Figure 2b, for a continuously changing field precession angle θ. The trajectory of the flagellum is displaced by 200 μm along *y*-axis for clarity. b–d) Decomposition of the trajectory described by the head and flagellum in (a) to rectangular components (*X*–*Y*). b) The plot describes the *X*–*Z* plane of oscillation R_{xz} ("top") and *Y*–*Z* plane of oscillation R_{yz} ("bottom") for the respective swimmer's head and flagellum for varying field precession θ. c) Phase difference between the oscillation of head and flagellum in (I) *X*–*Z* plane as ϕ_{xz} and (II) *Y*–*Z* plane as ϕ_{yz} for varying θ at two actuation frequencies (3 and 4 Hz). d) Calculated swimmer velocities normalized to the maximum swimming speed for varying θ at two actuation frequencies (3 and 4 Hz).

© 2020 The Authors. Published by WILEY-VCH Verlag GmbH & Co. KGaA, Weinheim

to the Cartesian system (R, ϕ). Hereby, we express the trajectory of the swimmer moving in the Z-direction, as shown in **Figure 3**a, into its orthogonal components in the X–Z plane (R_{xz}, ϕ_{xz}) and the Y–Z plane (R_{yz}, ϕ_{yz}), as shown in Figure 3b. Going by this principle, we approximate the swimmer's motion in each plane as a bending wave propagating across its two distal ends.[30] We further represent the oscillations of the head (h) and the flagellum (f) in terms of their relative phase difference in the two planes of oscillations. Hereby, we define ϕ_{xz} and ϕ_{yz} as the constant phase differences between the head and the flagellum for a given field precession θ in the two respective planes as,

$$\phi_{xz} = \phi_{\mathrm{h},x(z=0)} - \phi_{\mathrm{f},x(z=L)} \tag{1}$$

$$\phi_{yz} = \phi_{\mathrm{h},y(z=0)} - \phi_{\mathrm{f},y(z=L)} \tag{2}$$

where L is the length of the swimmer. We analyze the oscillations in Figure 3b for continuously increasing values of field precession angles ($\theta = 50°$–$90°$) to derive two notable observations. In the X–Z plane, the oscillation of the flagellum leads over that of the head at $\theta = 50°$ i.e., $\phi_{xz} < 0$. Finally, at $\theta = 90°$, a phase crossover occurs and the head takes over the flagellum, i.e., $\phi_{xz} > 0$. In contrast, in the Y–Z plane, the flagellum always has a phase lead over the head, i.e., $\phi_{xz} < 0$, whereas this lead increases to 180° as θ increases from 50° to 90°. This means that the bending wave propagating along the swimmer's body changes its direction when triggered by a change in field precession. Quantitatively, we measure the phase response of the swimmer at two different frequencies ($f = 3$ and 4 Hz) in terms of ϕ_{xz} and ϕ_{yz}, respectively, as shown in Figure 3c. In terms of oscillation amplitudes, at $\theta = 50°$, for both the X–Z and Y–Z planes, the flagellum has a higher amplitude than the head, i.e., $R_{\mathrm{h},x} < R_{\mathrm{f},x}$ and $R_{\mathrm{h},y} < R_{\mathrm{f},y}$, whereas at $\theta = 90°$, the head dominates the flagellum, i.e., $R_{\mathrm{h},x} > R_{\mathrm{f},x}$ and $R_{\mathrm{h},y} > R_{\mathrm{f},y}$ as shown in Figure S1g, Supporting Information.

Hereon, we approximate the propagation of the bending wave in the swimmer by considering the overall induced oscillation along its body as the sum of two oscillations that differ both in amplitude and in phase. Previously, Namdeo et al. modeled a bidirectional swimmer with a magnetic head and a flexible flagellum to undergo motion reversal, premised upon this superposition.[30] Mathematically, the overall deformation of a swimmer moving along the Z-direction can be decomposed as the sum of magnetic oscillations and drag-induced oscillations occurring in both X–Z and Y–Z planes[30]

$$x(z,t) = a_1 \sin(\omega t)\left(\frac{z}{L}\right) + a_2 \sin(\omega t + \phi_{xz})\left(\frac{z}{L}\right)^m \tag{3}$$

$$y(z,t) = a_3 \sin(\omega t)\left(\frac{z}{L}\right) + a_4 \sin(\omega t + \phi_{yz})\left(\frac{z}{L}\right)^m \tag{4}$$

where ϕ_{xz} and ϕ_{yz} are the phase differences described in Equation (1) and (2), respectively, and m is a curvature factor.[30] Further, a_1 and a_3 represent the amplitudes of rigid-body magnetic rotation, whereas a_2 and a_4 represent that of the drag-induced oscillation. As our magnetic head dominates the magnetic response (Table 1), we approximate the rigid-body rotation to be dominantly contributed by the head. At the same time, the undulatory motion of the flagellum is dominated by the drag-induced deformation. Based on this supposition, we approximate the two amplitudes of oscillations at the two distal ends of the swimmer, i.e., $R_{\mathrm{h},i}$ and $R_{\mathrm{f},i}$ ($i = x,y$, as shown in Figure S1g, Supporting Information), to be the driving amplitudes a_j ($j = 1$–4) of the two oscillatory components in Equation (3) and (4).

Next, the propulsive forces generated by the swimmer in X–Z and Y–Z planes can be, respectively, evaluated using the resistive force theory with the following expressions[30,33]

$$F_Z(x) = \int_0^L C_{\|}\left\{\left(\frac{C_\perp}{C_{\|}} - 1\right)\frac{\mathrm{d}x}{\mathrm{d}t}\frac{\mathrm{d}x}{\mathrm{d}z} - V_z(x)\right\}\mathrm{d}l \tag{5}$$

$$F_Z(y) = \int_0^L C_{\|}\left\{\left(\frac{C_\perp}{C_{\|}} - 1\right)\frac{dy}{dt}\frac{dy}{dz} - V_z(y)\right\}dl \tag{6}$$

where $C_{\|}$ and $C_\perp$ are the drag coefficients per unit length dl of the swimmer in tangential and normal directions, respectively. Note that V_z represents terminal swimmer velocity in the Z-direction, which has two components, $V_z(x)$ and $V_z(y)$, as individual contributions from the swimmer deformations in X–Z and Y–Z planes, respectively. For an equilibrium condition, we evaluate the terminal velocity by considering the net force to be zero. Hereby, we substitute Equation (3) and (4) in Equation (5) and (6) to yield the expressions of $V_z(x)$ and $V_z(y)$ as

$$V_Z(x) = \pi\left(\frac{C_\perp}{C_{\|}} - 1\right)\frac{R_{\mathrm{h},x}R_{\mathrm{f},x}}{L^2}\sin(\phi_{xz})\left(\frac{m-1}{m+1}\right)\frac{L}{f} \tag{7}$$

$$V_Z(y) = \pi\left(\frac{C_\perp}{C_{\|}} - 1\right)\frac{R_{\mathrm{h},y}R_{\mathrm{f},y}}{L^2}\sin(\phi_{yz})\left(\frac{m-1}{m+1}\right)\frac{L}{f} \tag{8}$$

where f is the actuation frequency. Therefore, the swimmer can reverse its direction when the phase difference across its two oscillating ends changes sign, which in turn can be triggered by a change in field precession angle. Next, we estimate the swimming velocities for our range of field precession values by substituting the reported values in Figure 3c and S1g in Equation (7) and (8). Finally, we combine the two contributions of the swimming velocities in X–Z and Y–Z planes to compute the net swimming velocity, i.e., the velocity of the bending wave traveling along the swimmer's body as

$$V_Z = V_Z(x) + V_Z(y) \tag{9}$$

We hereby report the net swimming velocity for all the range of applied θ normalized to the maximum swimming speed, as shown in Figure 3d. It can be clearly seen that swimming velocity V_z tends to increase from a dominant negative range at $\theta = 50°$, toward a positive value at $\theta = 90°$. Furthermore, the zero crossings occur close to $\theta = 80°$–$90°$, which is higher than our observed range of $\theta = 70°$–$80°$ where motion reversal occurs. We attribute the small difference in the value of observed and calculated zero crossings to the approximate swimming profiles adopted during the analysis and calculation of velocities. As we discover precession angle of the field to be the requisite stimulus for motion reversal of our swimmer, we proceed with our experimental investigation to study its influence on different swimmer designs.

© 2020 The Authors. Published by WILEY-VCH Verlag GmbH & Co. KGaA, Weinheim

2.4. Single Microswimmer Demonstrating Motion Reversal with Changing Precessing Field

To validate the reversible motion, we subjected our swimmers to changing field precession angles, keeping the frequency fixed. Akin to the previous observation of the swimmer's vertical motion in Figure 2a, the side view of the swimmer also shows different arc-shaped profiles for varying precessions. **Figure 4**a,b shows different time-stamps for the swimmers and their respective shapes, as they perform forward or backward motion. Each time-stamp here depicts overlapped images of the swimmer undergoing successive swimming strokes to capture the arc-shaped deformations. For instance, we consider the Type I swimmer first and depict the intersection points by superimposing the swimmer's successive swimming strokes. These nodal points (marked with colored crosses, Figure 4a) appear as stationary points, around which both the distal ends of the swimmer, i.e., the head and the flagellum, oscillate. Here, the swimmer's head ascends with a bigger amplitude of oscillation than the flagellum while moving forward at 90° precession. In contrast, the amplitude of the swimmer's head gradually decreases while the flagellum gains a greater amplitude of ascent at lower precessions ($\theta = 50°$), as the swimmer moves backward (Movie S2, Supporting Information).

Thereon, we systematically characterize the precession-speed characteristics for both the swimmer types with the magnetic field rotation applied at 12 Hz, as shown in Figure 4c. We find that the Type II swimmer undergoes motion reversal at a higher precession value ($\theta_{\text{t-II}} \approx 70°$) than that of Type I ($\theta_{\text{t-I}} \approx 60°$). We relate this variance in switching angles, particularly for the low-precession response of the two swimmer types, to the design metrics discussed earlier in Section 2.1. As the head and flagellum of the swimmers share a common rigid link, having a larger head–flagellum tilt γ results in a greater part of the swimmer's arc across its principal axis of rotation. This is evident from the swimmer profiles in Figure 4a,b ("red" and "yellow"), where the Type II swimmer oscillates with a greater part of the flagellum across the principal axis than the Type I swimmer. Hence, we deduce that due to its larger predefined tilt angle γ, the Type II swimmers assume this profile and oscillate with a greater amplitude of oscillation at the low-field precession θ, when compared with the Type I swimmers. The difference in the amplitude of oscillation suggests that for a specified field precession θ, the contribution of the flagellum in the case of Type II swimmers is higher than that of Type I. This leads to a disparity in switching points for motion reversal of the two swimmer designs as θ changes. The effect of having a larger predefined tilt γ in Type II swimmers is further intensified due to a higher misalignment δ observed in a static magnetic field, compared with that of Type I (Table 1). This misalignment is due to the fact that the flagellum of Type II swimmers possesses a slightly higher Fe content, due to a more consistent distribution of small iron filaments, caused by fabrication precision (see details in Experimental Section). Together, an overall larger γ'' ($\gamma'' = \delta + \gamma'$) in Type II swimmers further leads to a larger $R_{\text{f},i}$ ($i = x,y$), i.e., a larger Type II flagellum contribution (refer to Equation (3) and (4)) to the backward propulsion than the Type I flagellum. As a result, motion reversal occurs earlier in Type II than Type I swimmers as θ decreases from 90° to 50°. This presents the possibility of moving both types of swimmers in opposite directions with a common magnetic actuation. This shift in the general trend of precession-speed characteristics (as shown in Figure 4c) between Type I and Type II is further corroborated by their difference in switching points. Further, we also find that the Type II swimmers do not synchronize well with the rotating field when the precession angle is lowered below 55°, whereas the Type I swimmers could respond to precession angles well below 50°. This follows from the fact that the higher γ for Type II swimmers (Table 1), imposed by the magnetic moment of the head, provides lower tolerance for it to maintain stable axial rotation at lower θ. Further, as we investigate the two swimmers at high actuation frequencies, we find the influence of their respective cut-off frequencies. Hereby, for $f > 20$ Hz, we define the tolerance limits for Type I swimmer to be $\theta = 50°$ and Type II swimmer to be $\theta = 60°$ for stable axial rotations.

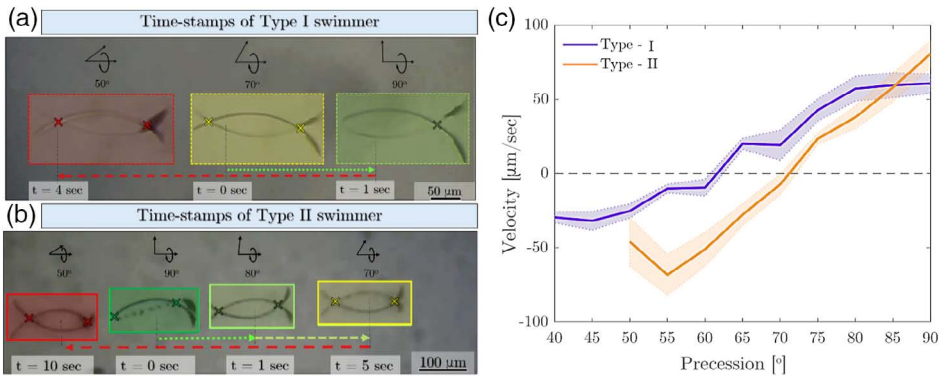

Figure 4. a,b) Time-lapse images of the microswimmer's motion under varying precessions of magnetic field ($B = 5$ mT), applied at a constant frequency ($f = 12$ Hz). The color scheme for the box enclosing the microswimmer represents green for forward motion, red for backward motion, and light green yellow for a transition between the two. The time-stamps depict successive swimming strokes of a) Type I and b) Type II swimmers, respectively. The similarly colored crosses represent stationary points on the rotation axis. c) A plot of the velocity profile of both the swimmer variants (Type I and II) for varying precession angles of the rotational magnetic field ($B = 5$ mT) applied at a constant frequency of 12 Hz, showing the forward–backward velocity component. The similarly colored shaded region represents the standard deviation at each data point.

© 2020 The Authors. Published by WILEY-VCH Verlag GmbH & Co. KGaA, Weinheim

2.5. Two Microswimmers Showing Parallel and Antiparallel Motion

Next, we characterize the swimming properties of the two swimmer types over a frequency range, for all possible values of the precessing fields (5 mT). We observe that both types of swimmers move forward at higher values of the field precession angle ($\theta > 80°$) and switch to backward propulsion ($\theta < 60°$) at their respective switching precession angles, as shown in **Figure 5**a,b. The design of swimmers can be utilized to differentiate the motions of these swimmers. Specifically, the transition for Type I swimmers occurs at $\theta = 70°$, below which they predominantly propel backward and reach maximum backward velocity at $\theta = 50°$ (Movie S3, Supporting Information). In contrast, the Type II swimmers, in general, maintain the trend of backward motion in the range of $\theta = 60°$–$70°$ and forward motion in the range of $\theta = 80°$–$90°$ (Movie S4, Supporting Information). In addition, we notice that a few Type I swimmers exhibit forward motion at $\theta = 70°$, albeit with lower displacements compared with their body length (Movie S3, Supporting Information). We reason that close to the switching point $\theta_{t\text{-}I} = 70°$, the motion is very sensitive to geometry and even slight variations in the released flagellar pattern could affect the motion direction. Another noteworthy observation is that the Type I swimmers either show no overall motion or forward motion with lower speeds compared with their length at low frequencies when $\theta = 60°$. On the contrary, nearly all the Type II swimmers swim backward at $\theta = 60°$ with higher velocities even at low frequencies, thus making it a suitable control input to achieve antiparallel motion of the two swimmer types.

From the observations in Figure 4c and 5a,b, we can conclude that not only do the two swimmers have different transition points in terms of precession, but also in terms of frequency, whereby they achieve different peak velocities. This duality can diversify the control strategies used to control multiple microrobots, as previously reported approaches are influenced

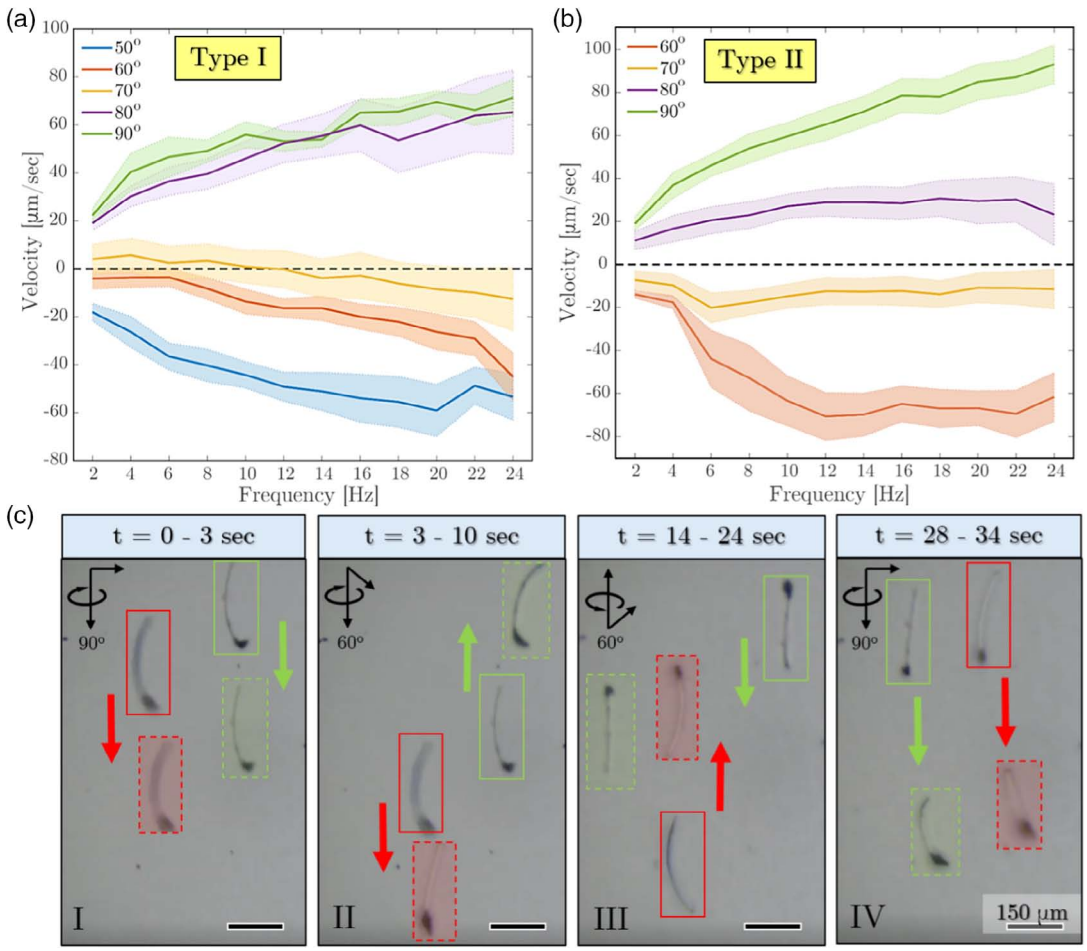

Figure 5. a,b) Forward and backward swimming velocities of the two swimmer variants, a) Type I and b) Type II over varying precession angles and frequencies of magnetic actuation. The similarly colored shaded region represents the standard deviation at each data point. c) Time-lapse sequence depicting the independent control of two swimmer (color scheme: Type I marked red and Type II marked green) variants under a common magnetic actuation: where (I) swimmers initially move in parallel motion (90°), (II) one of the swimmers switches direction and they start to drift away from each other (60°), (III) under reversal of the field direction they move toward each other (60°) and Type II swimmer drifts due to its proximity to the substrate, and (IV) they come together again continue to move in parallel (90°). For each swimmer, the solid line box represents the previous position, whereas the dashed line box represents the next position.

© 2020 The Authors. Published by WILEY-VCH Verlag GmbH & Co. KGaA, Weinheim

by either changing frequency,[23,26,34] predefined magnetic anisotropy,[24,25,35] or complex path-planning methods.[36,37] Based on the findings of different switching points, $\theta_{\text{t-I}}$ and $\theta_{\text{t-II}}$ in Figure 4c, we exploit field precession for the multiagent control of the two types of swimmers (Movie S5, Supporting Information). Figure 5c shows the time-stamps of the two swimmers, moving in parallel formation at $\theta = 90°$ (5 mT, 9 Hz), before they switch into antiparallel motion at $\theta = 60°$, and finally moving in a parallel trajectory again at $\theta = 90°$. Future work in this direction will be extended to the precession-driven actuation of multiple swimmers differing in tilt, geometry, and magnetization, thus paving the way for convergent and divergent formations of agents to accomplish co-operative tasks.

3. Conclusions

In conclusion, we have demonstrated the bidirectional propulsion of arc-shaped microswimmers, by exploiting their unique geometry to generate different dynamic conformations under precessing magnetic fields. We establish the extent to which the swimmers can synchronize to the changing field precession, based on their dipole orientation in a static magnetic field and their intrinsic geometry. Also, we have shown that structurally dissimilar swimmers with similar material composition can produce dramatically different magnitudes of forward–backward motion. This similarity in composition makes it convenient to fabricate a wide range of microswimmers, all with different magnetic responses but the same magnetic content in the same number of photolithographic steps, thereby broadening the scope of batch fabrication. Finally, we have shown an example of the independent actuation of the two swimmer types, making them move in both the same and opposite directions, without altering either the direction of actuation or its frequency. Consequently, formations of such independently controlled swimmers can be deployed successfully for micromanipulation tasks in cluttered and confined biological environments.

4. Experimental Section

Design and Fabrication: The microswimmer was composed of a rigid triangular head and a thin long flagellum. The head was designed to dominate the magnetic response, whereas the flagellum was designed to stabilize motion under the rotating magnetic field and contribute to the magnetic response secondarily. The fabrication process included three steps, as shown in Figure S1d, Supporting Information. First, we deposited a sacrificial layer (15 nm Cr and 100 nm Cu) on a silicon wafer, which allowed the complete release of the microswimmer after fabrication. Second, we patterned the flagellum by photolithography and e-beam evaporation (30 nm SiO, 90 nm SiO_2, 10 nm Fe, and 10 nm SiO_2). The flagellum was 180 µm long and 6 µm wide. The swimmer formed an arc-shaped flagellum after release due to the different thin-film stresses in the SiO/SiO_2 bilayer.

Third, we patterned the head and the small rigid filaments together by photolithography and e-beam evaporation (150 nm SiO_2, 10 nm Cr, 20 nm Fe, and 15 nm SiO_2). The head was 20 µm wide and 40 µm long. The relative alignment in photolithography ensured that the head overlapped with the flagellum for good adhesion and included the periodic pattern of small filaments on the flagellum. After fabrication, the microswimmers were released from the substrate in a copper etchant APS-100 (Transene) (Figure S1c and S1e,f, Supporting Information). Photoresist AZ 5214E (MicroChemicals) was used for photolithography. The materials for e-beam evaporation were purchased from the Kurt J. Lesker company.

Based on fabrication, the head dominated the magnetic response and remained parallel to the instantaneous direction of the field due to the iron layer, and the flagellum served to stabilize the rotating motion under the precessing magnetic field and contributed less to the magnetic response. This secondary contribution led to a small magnetic misalignment angle δ between the head and the easy axis of the swimmer, as defined in the article. We noticed that the Type I swimmer had a smaller misalignment angle than that of the Type II swimmer. This difference was attributed to the slightly lower iron content in the flagellum of Type I. Given the same area by design, the lower tilt angle of the filaments in Type I resulted in a narrower width i.e., a smaller critical dimension of 1.5 µm (2.1 µm for Type II), which was more sensitive to the pattern transfer process.

Experimental Setup and Workspace Design: A Helmholtz coil system was used for wireless microrobot propulsion. The system consisted of three pairs of coils placed orthogonally to enable a region of a uniform magnetic field of up to 5 mT at its center (Figure S1a, Supporting Information). A chamber made of polydimethylsiloxane was designed to be our magnetic workspace, and it provided us with a working volume of $\approx$1 cm^3 in water (Figure S1b, Supporting Information). The current supplied to the system was controlled and amplified by the XenusPlus EtherCAT (XE2-230-20, Copley Controls, Canton, USA). The system was controlled by a custom-made program based on C++, which facilitated current control to the coils and enabled image acquisition from a CMOS camera (Point Grey Research Inc., Blackfly GigE Vision, pixel size = 3.75 µm). Further, the coils were programmed to provide an oscillating magnetic field at any precession angle, with the case of 90° corresponding to a high-applied precession angle.

Supporting Information

Supporting Information is available from the Wiley Online Library or from the author.

Acknowledgements

S.M. and Q.J. contributed equally to this work. This work was supported by funds from The Netherlands Organization for Scientific Research (Innovational Research Incentives Scheme-VIDI: SAMURAI, project No.14855) and the National Science Foundation CMMI-1635443. The authors thank Ugo Siciliani de Cumis and Jakub Sikorski for their assistance in assembling the experimental hardware.

Conflict of Interest

The authors declare no conflict of interest.

Keywords

bioinspired microswimmers, biomimetics, magnetic propulsions, precessing fields, reversible motions, swarm robotics

Received: April 1, 2020
Revised: April 29, 2020
Published online:

[1] E. Lauga, T. R. Powers, *Rep. Prog. Phys.* **2009**, *72*, 096601.
[2] Y. Magariyama, M. Ichiba, K. Nakata, K. Baba, T. Ohtani, S. Kudo, T. Goto, *Biophys. J.* **2005**, *88*, 3648.
[3] S. Bubendorfer, M. Koltai, F. Rossmann, V. Sourjik, K. M. Thormann, *Proc. Natl. Acad. Sci.* **2014**, *111*, 11485.

© 2020 The Authors. Published by WILEY-VCH Verlag GmbH & Co. KGaA, Weinheim

[4] S. M. Vater, S. Weiße, S. Maleschlijski, C. Lotz, F. Koschitzki, T. Schwartz, U. Obst, A. Rosenhahn, *PLoS One* **2014**, *9*, e87765.
[5] M. Hintsche, V. Waljor, R. Großmann, M. J. Kühn, K. M. Thormann, F. Peruani, C. Beta, *Sci. Rep.* **2017**, *7*, 1.
[6] R. Sivakumar, P. Tholeti, R. R. Dhanusu, A. Benziger, P. Natarajan, *Matters* **2016**, *2*, e201610000010.
[7] K. Shiba, D. Shibata, K. Inaba, *Br. J. Exp. Biol.* **2013**, *217*, 986.
[8] M. Kottgen, A. Hofherr, W. Li, K. Chu, S. Cook, C. Montell, T. Watnick, *PLoS One* **2011**, *6*, e20031.
[9] K. Ishimoto, H. Gadêlha, E. A. Gaffney, D. J. Smith, J. Kirkman-Brown, *Phys. Rev. Lett.* **2017**, *118*, 124501.
[10] B. J. Nelson, I. K. Kaliakatsos, J. J. Abbott, *Annu. Rev. Biomed. Eng.* **2010**, *12*, 55.
[11] A. Ghosh, P. Fischer, *Nano Lett.* **2009**, *9*, 2243.
[12] A. Ghosh, D. Paria, H. J. Singh, P. L. Venugopalan, A. Ghosh, *Phys. Rev. E* **2012**, *86*, 031401.
[13] Y. Alapan, O. Yasa, B. Yigit, I. C. Yasa, P. Erkoc, M. Sitti, *Annu. Rev. Control Robot. Auton. Syst.* **2019**, *2*, 205.
[14] J. Bastos-Arrieta, A. Revilla-Guarinos, W. E. Uspal, J. Simmchen, *Front. Robot. AI* **2018**, *5*, 97.
[15] R. Fernandes, M. Zuniga, F. R. Sassine, M. Karakoy, D. H. Gracias, *Small* **2011**, *7*, 588.
[16] L. Zhang, J. J. Abbott, L. Dong, B. E. Kratochvil, D. Bell, B. J. Nelson, *Appl. Phys. Lett.* **2009**, *94*, 064107.
[17] A. Barbot, D. Decanini, G. Hwang, *Sci. Rep.* **2016**, *6*, 19041.
[18] A. Ghosh, D. Dasgupta, M. Pal, K. I. Morozov, A. M. Leshansky, A. Ghosh, *Adv. Funct. Mater.* **2018**, *28*, 1705687.
[19] H.-W. Huang, T.-Y. Huang, M. Charilaou, S. Lyttle, Q. Zhang, S. Pané, B. J. Nelson, *Adv. Funct. Mater.* **2018**, *28*, 1802110.
[20] H.-W. Huang, F. E. Uslu, P. Katsamba, E. Lauga, M. S. Sakar, B. J. Nelson, *Sci. Adv.* **2019**, *5*, eaau1532.
[21] I. S. M. Khalil, H. C. Dijkslag, L. Abelmann, S. Misra, *Appl. Phys. Lett.* **2014**, *104*, 223701.
[22] L. Zhang, J. J. Abbott, L. Dong, K. E. Peyer, B. E. Kratochvil, H. Zhang, C. Bergeles, B. J. Nelson, *Nano Lett.* **2009**, *9*, 3663.
[23] I. S. M. Khalil, A. F. Tabak, Y. Hamed, M. E. Mitwally, M. Tawakol, A. Klingner, M. Sitti, *Adv. Sci.* **2017**, *5*, 1700461.
[24] S. Tottori, B. J. Nelson, *Small* **2018**, *14*, 1800722.
[25] H.-W. Huang, Q. Chao, M. S. Sakar, B. J. Nelson, *IEEE Robot. Autom. Lett.* **2017**, *2*, 727.
[26] I. S. M. Khalil, A. F. Tabak, Y. Hamed, M. Tawakol, A. Klingner, N. E. Gohary, B. Mizaikoff, M. Sitti, *IEEE Robot. Autom. Lett.* **2018**, *3*, 1703.
[27] R. Schuech, T. Hoehfurtner, D. Smith, S. Humphries, *Proc. Natl. Acad. Sci.* **2019**, *116*, 14440.
[28] M. A. Constantino, M. Jabbarzadeh, H. C. Fu, R. Bansil, *Sci. Adv.* **2016**, *2*, e1601661.
[29] B. Liu, M. Gulino, M. Morse, J. X. Tang, T. R. Powers, K. S. Breuer, *Proc. Natl. Acad. Sci.* **2014**, *111*, 11252.
[30] S. Namdeo, S. N. Khaderi, P. R. Onck, *Phys. Rev. E* **2013**, *88*, 043013.
[31] J. Cools, Q. Jin, E. Yoon, D. A. Burbano, Z. Luo, D. Cuypers, G. Callewaert, D. Braeken, D. H. Gracias, *Adv. Sci.* **2018**, *5*, 1700731.
[32] V. A. Bolaños Quiñones, H. Zhu, A. A. Solovev, Y. Mei, D. H. Gracias, *Adv. Biosyst.* **2018**, *2*, 1800230.
[33] J. Gray, G. J. Hancock, *Br. J. Exp. Biol.* **1955**, *32*, 802.
[34] F. Bachmann, K. Bente, A. Codutti, D. Faivre, *Phys. Rev. Appl.* **2019**, *11*, 034039.
[35] P. Mandal, V. Chopra, A. Ghosh, *ACS Nano* **2015**, *9*, 4717.
[36] A. Denasi, S. Misra, *IEEE Robot. Autom. Lett.* **2018**, *3*, 218.
[37] F. Ongaro, S. Pane, S. Scheggi, S. Misra, *IEEE Tran. Robot.* **2019**, *35*, 174.

© 2020 The Authors. Published by WILEY-VCH Verlag GmbH & Co. KGaA, Weinheim